Motion resistance modelling and validation in winter conditions with varying air drag

Motion Resistance Modeling and Validation in Winter Conditions with Varying Air Drag

M. Askerdal[a,b], J. Fredriksson[b], L. Laine[a,c] and F. Bruzelius[c]

[a]Department of Vehicle Motion Management, AB Volvo, Sweden;
[b]Department of Electrical Engineering, Chalmers University of Technology, Sweden;
[c]Department of Mechanics and Maritime Sciences, Chalmers University of Technology, Sweden;

ARTICLE HISTORY
Compiled December 2, 2024

ABSTRACT
Range prediction is vital for battery electric vehicles, and the main source of errors in range prediction is often the uncertainty in motion resistance. Rig and wind tunnel measurements can be used to find the motion resistance of a specific vehicle combination under specified weather conditions. However, real-life variation of the operating conditions of heavy-duty vehicles makes testing impractical. This paper proposes and validates a model of motion resistance with parameters adapted to actual road weather conditions. The model is validated in winter conditions with varying wind, using a vehicle equipped with a wind sensor. The results show that the proposed model captures the motion resistance with high accuracy. Results also indicate that it is crucial to take weather effects into account when modeling motion resistance, particularly in winter conditions.

KEYWORDS
Air drag; motion resistance; modeling; rolling resistance; winter;

1. Introduction

Climate change is the root cause for regulations of CO_2 emissions. In the EU, maximum average CO_2 emission limits, [1], have been set on vehicle fleet level following the Paris agreement, [2]. OEMs that sell vehicles with a higher average CO_2 emission than the limit will be penalized. Several OEMs have chosen to speed up the development and introduction of battery electric vehicles as they are zero-emission vehicles and thus can significantly reduce the fleet average CO_2-emission level. Battery electric vehicles have many other advantages compared to fossil fuel-driven vehicles. They are, for example, more energy efficient, more silent, and often cheaper to operate, [3,4]. However, even though batteries are continuously improving, the effective driving range is still shorter compared to a fossil fuel-driven vehicle, [4]. The charging time is long, and the public charging infrastructure is far behind. Altogether, these disadvantages demand precise range prediction for enabling effective mission planning, avoiding unwanted stops, and range anxiety, [5].

Range prediction is about comparing the effective amount of energy stored in the

CONTACT M. Askerdal. Email: mikael.askerdal@volvo.com

battery, with the predicted energy consumption for driving the road ahead. Vehicle energy losses can be divided into auxiliary system losses, powertrain losses, and motion resistance losses. The motion resistance losses are usually divided into grade resistance losses, rolling resistance losses, and air drag losses.

With knowledge of the vehicle mass and the road grade, the grade resistance can be computed accurately. In a way, this makes grade resistance the simplest motion resistance term to model since it is only affected by the environment through the road grade that can be considered to be static. Low-fidelity measurements from many different vehicles can be used to estimate road grade with high accuracy, [6].

Rolling resistance is directly and indirectly affected by weather and road surface conditions. The direct effect mainly comes from resistance that is induced by displacing water or snow on the road surface or compression of soft road surfaces. Indirect effects include tire heating or cooling, for example, from ambient air and the road surface. Colder ambient air and road surface cools the tire more and lower tire temperature decreases the tire pressure. Both tire temperature and tire pressure have a strong correlation with rolling resistance, e.g., [7,8].

Air drag is affected by both the air density and the wind conditions. Air density can be calculated with fairly good precision from the ambient temperature and air pressure, [9], which most vehicles can measure. With knowledge of air humidity, the precision of the air density determination can be improved even more, especially in warm climates, where air can carry a higher degree of steam. When it comes to wind conditions, the effect on air drag is twofold, it changes the air speed relative to the vehicle, as well as the air attack angle. This is anticipated in [10], where it is argued that high-resolution wind information at the road level is necessary to accurately calculate the energy consumption of air drag. This is exemplified by showing how air drag is reduced in tail-wind conditions. The question of how to deal with the influence of crosswinds is not mentioned except that it affects the aerodynamic coefficient. Also, [11] has made an attempt to include weather information in a grey box vehicle energy consumption model. This model takes wind speed into account but lacks the influence of crosswinds. This can perhaps be explained by the model being developed for cars that are relatively insensitive to crosswinds. The crosswind effect on air drag for a bus has been described by an empirical model in [12]. In that paper, the model is fitted to wind tunnel measurements without any real explanation of the effect. An attempt to explain the effect of crosswind on air drag through physical reasoning together with crosswind sensitive models for different heavy-duty vehicle combinations can instead be found in [13].

In this paper, a motion resistance model adapted to winter conditions is proposed. The model includes rolling resistance and air drag. The rolling resistance model combines previous models proposed in the literature, while the air drag model builds on the models proposed in our previous work, [13]. The model is validated using measurements from a vehicle equipped with a wind sensor running on an ice track in winter conditions. The results highlight the importance of taking weather aspects into account in motion resistance models.

2. Modeling

This section presents the proposed motion resistance model. The motion resistance model is based on Newton's law, i.e.

$$ma(t) = F_{trac}(t) - F_{mr}(t), \tag{1}$$

where m is the vehicle mass, $a(t)$ the vehicle acceleration, $F_{trac}(t)$ the traction force and $F_{mr}(t)$ the motion resistance force. The motion resistance force is defined as the sum of the grade resistance, $F_g(t)$, air drag forces, $F_a(t)$, and rolling resistance, $F_r(t)$

$$F_{mr}(t) = F_g(t) + F_r(t) + F_a(t). \tag{2}$$

In the literature, e.g., [14–16], the effect of weather like wind and temperature is often neglected and the road is assumed to be flat, resulting in a total motion resistance force as:

$$F_{mr}(t) = \frac{1}{2}\rho C_d A v_v^2(t) + mgC_r, \tag{3}$$

where ρ is the air density, C_dA is the product of a constant air drag coefficient and the frontal area projection in the vehicle direction, $v_v(t)$ is the vehicle speed, g is the gravitational constant, and C_r is the rolling resistance coefficient. However, Computational Fluid Dynamics (CFD) simulations show that C_dA varies with changing air attack angle. The air attack angle is defined as:

$$\theta(t) = \arctan\left(\frac{|v_{wy}(t)|}{v_v(t) + v_{wx}(t)}\right) \tag{4}$$

where $v_{wx}(t)$ is the wind speed in the longitudinal direction and $v_{wy}(t)$ is the wind speed in the lateral direction in relation to the vehicle as illustrated in figure 1. The wind components and the relative air speed that stems from the vehicle speed, v_v, are added together to form the total relative air speed, v_a that attacks the vehicle at the angle θ.

Figure 1. Wind and air attack angle notations.

The effect of wind on air drag was investigated in our previous work, [13]. Here it was shown that a simple lumped parameter model of the air drag on the form:

$$F_a(t) = \frac{1}{2}\rho C_D A_p(\theta(t))(v_v(t) + v_{wx}(t))^2, \tag{5}$$

where C_D is the air drag coefficient, and $A_p(\theta(t))$ the front area projection in the vehicle motion direction can capture the effect of wind. The air drag coefficient C_D is a constant that must be determined from measurements or CFD simulations.

Figure 2 illustrates how C_dA values and area projections change with θ for three different vehicle combinations. Note that the CdA values are given as relative to $\theta = 0°$ of the tractor with semitrailer combination.

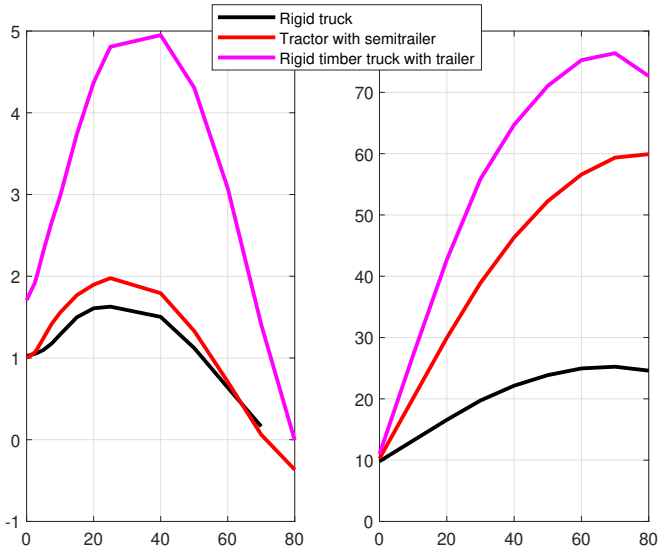

Figure 2. Area projection and relative C_dA for three vehicle combinations (taken from [13]).

When it comes to rolling resistance, it was argued in [17], that instantaneous rolling resistance (for a certain tire with a certain inflation level) is mainly a function of vehicle speed and tire temperature, $C_r(t) = C_r(v_v(t), T_{tire}(t))$ where $T_{tire}(t)$ is the tire temperature. The direct effect of weather is not visible in this model. The effect is more indirect and comes from the fact that tire temperature depends on road surface conditions and ambient temperature. This model is also confirmed by [18] where it is further stated that the rolling resistance is quadratic in vehicle speed. If running in stationary conditions, i.e. the tire temperature is constant, this results in the following model of the rolling resistance:

$$F_r(t) = mg(c_1 + c_2 v_v(t) + c_3 v_v^2(t)), \tag{6}$$

where c_1, c_2 and c_3 are constants coefficients. The rolling resistance coefficient $C_r(t) = F_r(t)/mg$, can now be described as:

$$C_r(t) = c_1 + c_2 v_v(t) + c_3 v_v^2(t). \tag{7}$$

If the coefficients c_1, c_2 and c_3 of (7) are adjusted to match the prevailing weather

conditions, combining (2), (5) and (6), results in the following weather-dependent motion resistance model:

$$F_{mr}(t) = F_g(t) + \frac{1}{2}\rho C_D A_p(\theta(t))(v_v(t) + v_{wx}(t))^2 + \\ + mg(c_1 + c_2 v_v(t) + c_3 v_v^2(t)). \tag{8}$$

where the grade resistance $F_g(t)$ can be modeled as $F_g(t) = mg\sin(\alpha(t))$ with $\alpha(t)$ being the road slope.

3. Method

The model proposed in the previous section is validated using real vehicle measurement data. Vehicle tests are performed with the purpose of parameterizing the rolling resistance model and validating the motion resistance model.

3.1. Test Vehicle

The test object used is a 4x2 Volvo FH tractor with a fully electric powertrain using four induction motors for traction. No trailer was used during the tests.

The vehicle is equipped with an anemometer for measuring air speed and air attack angle mounted on the roof of the cab as can be seen in figure 3. The wind sensor used is a 2-D Ultrasonic Anemometer from Thies CLIMA, which measures horizontal air speed and horizontal air direction. The vehicle was also equipped with Goodyear's

Figure 3. The test vehicle with an anemometer on the cab roof.

TPMS, capable of measuring the tire pressure as well as the tire temperature close to the rim. The vehicle mass is 9000 kg.

3.2. Test conditions

The tests were performed at the Colmis Proving Ground, Arjeplog, Sweden, on March 16, 2023. The road surface during the tests was scraped ice, i.e., ice plowed free from snow and then roughened by a grader that creates tracks in the ice surface. The result is a track surface that is more stable in changing winter conditions and with higher road friction compared to pure ice. The ambient conditions were a sunny, rather cold winter day. More exact data can be found in table 1, where data measured in the vehicle are compared to the data from the SMHI (Swedish Meteorological and Hydrological Institute) weather station located closest to the test site.

Table 1. Ambient conditions during the test day.

Type of condition	Measured values	SMHI values
Ambient temperature	-12 [$^{\circ}C$]	-12 [$^{\circ}C$]
Ambient pressure	N/A	970 [hPa]
Average wind speed	3.7 [m/s]	2.1 [m/s]
Average wind direction	303°	309°
Weather type	Clear sky	Clear sky

The air density, ρ, was computed, using [9], to be 1.29 kg/m^3 during the tests. The rather large deviation between the measured wind speed and the weather station wind speed can partly be explained by the fact that the closest weather station is located more than 11 km away from the ice tracks, and the weather situation may be different between the two locations. Another possible explanation is that the ice tracks are located on a lake without any obstacles that can shelter from the wind, while the weather station is located on land where trees, hills, and buildings may affect the measured wind speed.

3.3. Vehicle measurements

Two main types of vehicle measurements were conducted.

(1) Roll-out tests
(2) Ice circle tests at a constant velocity

The roll-out tests were conducted on a 2 km long straight handling track on the icy lake, see figure 4a. The truck was accelerated up to 50 km/h, and then the accelerator was released and the vehicle was free rolling until reaching a low speed. Driving was only permitted in one direction on the straight handling track, and hence, all roll-out tests were conducted in the south-to-north direction. The tests were also all starting from approximately 50 km/h. Higher velocities were not permitted on the lakes in order not to damage the ice surface.

Notice that the powertrain of the test vehicle does not have a clutch, but idle losses of the test vehicle's induction motors are considered negligible. In total, eight

successfully conducted roll-out tests were conducted with the purpose of finding the model parameters of the vehicle's velocity-dependent rolling resistance.

The ice circle tests were conducted by running at constant speed in a circle with a radius of approximately 240 m, see figure 4b. The purpose of these tests was to calibrate the anemometer and to verify the motion resistance model given by (8) in varying air drag that comes from the wind when running around the circle. The tests were repeated five times with different vehicle speeds, i.e. 10 km/h, 20 km/h, 30 km/h, 40 km/h and 50 km/h.

(a) straight handling track

(b) ice Circle

Figure 4. Examples of test track on scraped ice at Colmis Proving Ground. Pictures from Colmis web page, https://www.colmis.com/track/ice-tracks/

3.4. Wind sensor calibration

The wind sensor itself was calibrated before the tests, but the flow generated by the vehicle disturbs the airspeed at the sensor position. Therefore, the wind speed measurements need to be corrected for this disturbance. Two correction factors are introduced. The first correction factor, c_s relates the undisturbed longitudinal air speed in the simulations, $v_{axc} = 25$ m/s, to the simulated longitudinal air speed at the sensor location, v_{axm} through:

$$v_{axc}(t) = c_s(\theta_c(t))v_{axm}(t). \tag{9}$$

The second correction factor, c_t relates the undisturbed air attack angle in the simulations, θ_c, to the simulated air attack angle at the sensor location, θ_m through:

$$\theta_c(t) = c_t(\theta_c(t))\theta_m(t). \tag{10}$$

CFD simulations performed by the aerodynamic department at Volvo Trucks indicate that c_s and c_t do not depend on θ_c, i.e., c_s and c_t are constants, see Figure 5. This

implies that v_{axc} and θ_c can be modeled as being linear in the measured v_{axm} and θ_m.

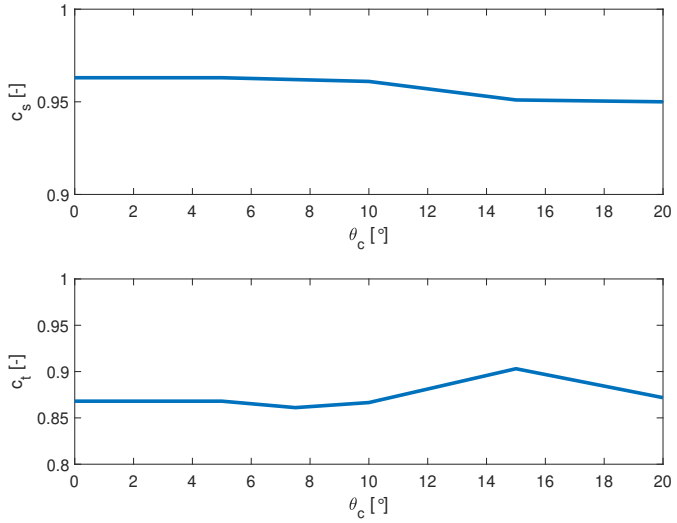

Figure 5. CFD simulations for illustrating the airspeed correction factors. Correction factors as function of air attack angle for an air speed of $v_{axc} = 25$ m/s.

Note that the wind sensor is measuring the relative air speed, v_{am}, rather than v_{axm}. The relation between v_{am} and v_{axm} can be described by:

$$v_{axm}(t) = cos(\theta_m(t))v_{am}(t). \tag{11}$$

The relation between v_{ac} and v_{axc} can be described similarly;

$$v_{axc}(t) = cos(\theta_c(t))v_{ac}(t). \tag{12}$$

By combining (9)-(12), and assuming that c_s and c_t are constants, the simulated undisturbed air speed, v_{ac}, can be computed from the measured v_{am} and θ_m according to:

$$v_{ac}(t) = \frac{c_s cos(\theta_m(t))v_{am}(t)}{cos(c_t\theta_m(t))}, \tag{13}$$

Based on equations (9) and (10), with constant coefficients c_s and c_t, a calibration scheme was determined to find the value of these coefficients. To support the calibration, a ground-fixed coordinate system was defined. In this coordinate system, the vehicle speeds can be described as

$$v_{vN}(t) = \cos(\theta_v(t))v_v(t), \tag{14a}$$

$$v_{vE}(t) = \sin(\theta_v(t))v_v(t), \tag{14b}$$

where $v_{vN}(t)$ and $v_{vE}(t)$ are the vehicle speeds in the two orthogonal directions, in this work north, N, and east, E. These directions, however, do not need to be aligned

with the geographical north and east directions. The vehicle heading in the ground fixed coordinate system is denoted $\theta_v(t)$ and illustrated in figure 6.

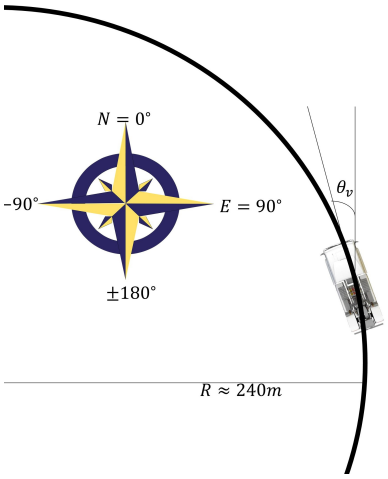

Figure 6. Vehicle heading in ground fixed coordinate system.

Note that when going around a circle, the vehicle, and hence the wind sensor, will slip in the lateral direction. In this case, as the circle radius is quite large (> 200 m) and the vehicle speed moderate (≤ 50 km/h), the lateral force, and hence the slip angle, should be small and has been neglected.

With the side slip neglected, the relative air speeds in the two directions, $v_{aN}(t)$ and $v_{aE}(t)$, can be described as

$$v_{aN}(t) = v_{vN}(t) + v_{wN}, \tag{15a}$$

$$v_{aE}(t) = v_{vE}(t) + v_{wE}, \tag{15b}$$

where v_{wN} and v_{wE} are the wind speeds in the north and east directions respectively. The wind speeds are assumed to be constant.

The ground-fixed relative air speeds can also be deducted from the calibrated measured air speed, $v_{ac}(t)$ and relative air direction, $\theta_c(t)$, according to

$$v_{aN}(t) = v_{ac}(t)\cos(\theta_v(t) + \theta_c(t)), \tag{16a}$$

$$v_{aE}(t) = v_{ac}(t)\sin(\theta_v(t) + \theta_c(t)). \tag{16b}$$

The vehicle direction on the ground fixed system, $\theta_v(t)$, can be found by assuming that the vehicle is traveling counterclockwise on a perfect circle with the radius R. Then by fixing the coordinate system such that the vehicle starts in the north direction, i.e. $\theta_v(0) = 0$, the vehicle direction can be described by:

$$\theta_v(t) = -\frac{1}{R}\int_0^t v_v(\tau)d\tau, \tag{17}$$

The wind speed components, $v_{wN}(t)$ and $v_{wE}(t)$ can now be computed by combining (9) - (17) to

$$v_{wN} = \frac{c_s v_{am} \cos(\theta_m) \cos(\theta_v + c_t \theta_m)}{\cos(c_t \theta_m)} - v_v \cos(\theta_v), \tag{18a}$$

$$v_{wE} = \frac{c_s v_{am} \cos(\theta_m) \sin(\theta_v + c_t \theta_m)}{\cos(c_t \theta_m)} - v_v \sin(\theta_v). \tag{18b}$$

The time dependency has been omitted in (18) for readability reasons.

By assuming that the wind is constant when going around the circle, the calibration constants, c_t, and c_s, can be found by minimizing the variance of the two wind speeds, v_{wN} and v_{wE}:

$$\arg\min_{c_t, c_s} var(v_{wN}) + var(v_{wE}). \tag{19}$$

The calibration scheme was applied using circle tests at different vehicle speeds, and the calibration coefficients were found using an exhaustive grid search. In figure 7, the calibrated wind speed components are compared with wind speed components computed from raw sensor signals. The c_s calibration coefficient makes the headwind speed component more or less symmetric around zero and the c_t calibration coefficient ensures that the amplitude of the crosswind speed is similar to the amplitude of the headwind.

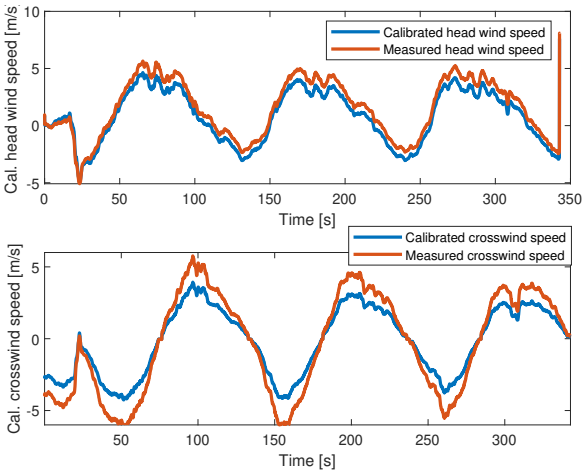

Figure 7. Comparison of wind component measures before and after calibration.

The calibration coefficients varied somewhat in the test conducted with different vehicle speeds according to table 2. The low variation in the values of c_s and c_t are consistent with CFD simulation results. The average values of c_s and c_t found from the tests in vehicle speeds between 20 and 50 km/h are selected to calibrate the measured wind speed and direction. It is worth noting that the coefficients for the lowest vehicle speed, $v_v = 10$ km/h, are treated as an outlier. A plausible reason for this outlier is that the linear calibration scheme in air attack angle was only validated

for $\theta < 25°$ in the CFD simulations. When running at 10 km/h vehicle speed, the prevailing wind conditions resulted in much larger air attack angles, see figure 8, and a possible explanation is that the linear calibration scheme does not work in these low vehicle speeds.

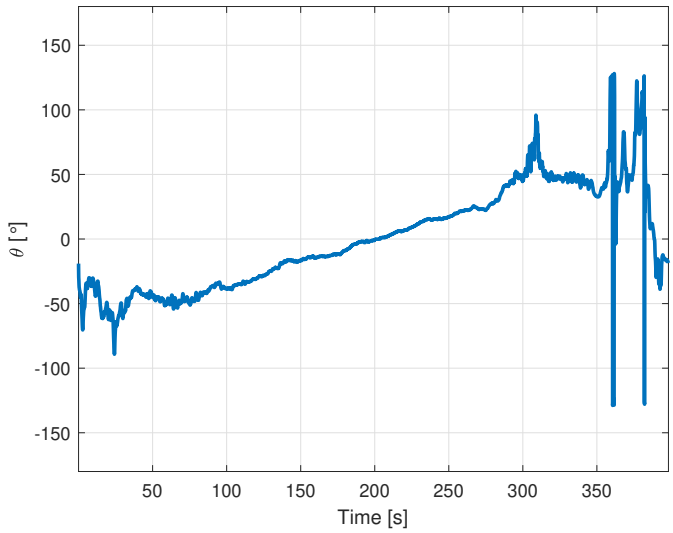

Figure 8. Air attack angles during ice circle test, vehicle speed = 10 km/h

Table 2. Calibration parameters from optimization.

	Vehicle speed v_v [km/h]					
	10	20	30	40	50	Used values
c_s [-]	0.75	0.97	0.95	0.94	0.90	0.94
c_t [-]	0.24	0.72	0.74	0.80	0.63	0.72

4. Results

As mentioned earlier, two different types of tests were performed; roll-out tests and circle tests. The purpose of the roll-out tests was to validate the rolling resistance model, (6), and the purpose of the circle tests was to validate the motion resistance model, (8).

4.1. Roll-out tests

The total motion resistance force, F_{mr}, during the roll-outs is, according to (1), proportional to the acceleration as:

$$F_{mr}(t) = -m\frac{dv_v(t)}{dt}. \tag{20}$$

As the test was conducted on ice on a lake, the grade resistance was zero, meaning that the rolling resistance force, $F_r(t)$, can be modeled as the difference between the motion resistance force, $F_{mr}(t)$, and the air drag $F_a(t)$

$$F_r(t) = F_{mr}(t) - F_a(t). \tag{21}$$

Since the roll-out tests were performed on the straight handling track and the wind direction was constant throughout the test, CFD computations were used to determine the air drag. Note, though, that since values from CFD simulations only were available for air attack angles up to 10° (blue line in figure 9), to get a model for C_dA values higher than that, extrapolation using the projection area was used, i.e. $C_dA(\theta) \approx C_D A_p(\theta)$ with C_D and $A_p(\theta)$ from equation (5) (red line in figure 9). This is in accordance with the models in [13]. The air drag properties for different air attack angles are then determined by how the projection area changes with the air attack angle. The result of this extrapolation is the red curve in figure 9.

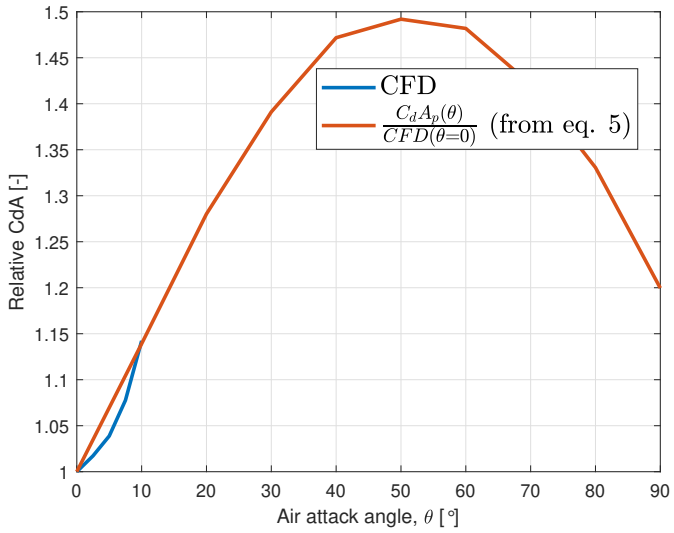

Figure 9. Comparison between CFD simulations and proposed air drag model for different air attack angles. The blue curve corresponds to C_dA from CFD simulations and the red curve corresponds to the model (5). The curves are normalized by the air drag at zero air attack angle.

Figure 10 shows an example of the roll-out tests. The blue line is the motion resistance force calculated from the total wheel force generated by the electric machines and the vehicle speed change (deceleration). The red line shows the modeled motion resistance. The other curves correspond to the modeled rolling resistance (yellow), the modeled air drag from vehicle speed (green), and the modeled air drag from the measured wind (magenta). As can be seen, the rolling resistance was the dominant motion resistance force during the roll-out tests.

The parameters c_1, c_2, and c_3 of the speed-dependent rolling resistance model were identified from roll-out tests through regression. The regression procedure minimizes the sum of the root mean square of the deviation between C_r computed from the measured F_r using equation (21) and a modeled rolling resistance coefficient $\hat{C}_r$, from

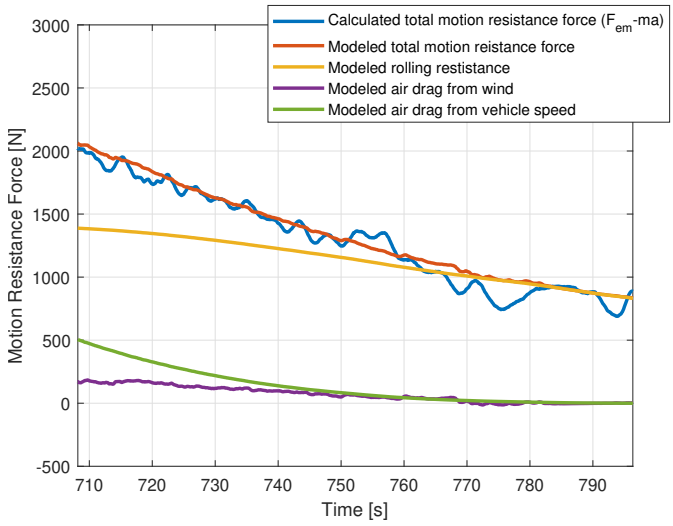

Figure 10. Roll-out test for rolling resistance model parameter identification.

equation (7):

$$\underset{c_1,c_2,c_3}{\arg\min} \sqrt{\frac{1}{N}\sum_{k=1}^{N}\left(\frac{F_r[k]}{mg} - (c_1 + c_2 v_v[k] + c_3 v_v[k]^2)\right)^2}, \tag{22}$$

where k is the sample number. All roll-out tests did not start at exactly the same vehicle speed and at low speeds, the measurements started to become very noisy, so the measurements used for the regression were limited to vehicle speeds between 15 and 45 km/h. The regression resulted in, $c_1 = 9.3{\cdot}10^{-3}$ (-), $c_2 = 9.0{\cdot}10^{-4}$ $(\mathrm{m/s})^{-1}$, and $c_3 = -3.1{\cdot}10^{-5}$ $(\mathrm{m/s})^{-2}$ when taking all roll-out tests into account. Figure 11 illustrates the speed-dependent transient rolling resistance model using the identified c_1, c_2, and c_3 parameters for vehicle speeds up to 50 km/h. There is clearly a strong vehicle speed dependency on the transient rolling resistance.

It shall be noted, though, that a small decrease in the total motion resistance was observed during the repeated roll-out tests. This is shown in figure 12, where two early roll-out tests are compared with two late roll-out tests. As can be seen, the motion resistance is clearly lower in the latter tests. The wind conditions during these tests were too similar to explain the deviation. Rolling resistance has been reported to decrease with tire temperature, [19,20], and it is hence more likely that the decrease in motion resistance comes from a decrease in rolling resistance due to tire heat-up during the tests.

4.2. Ice circle tests

The ice circle tests were used to verify the motion resistance model given by (8). Figure 13 compares the measured total motion resistance force, $F_{trac}(t) - ma(t)$, with a total motion resistance force modeled by (8). It also shows the individual motion resistance forces, i.e., air drag and rolling resistance forces, modeled by (5), and (6) respectively, when driving at three different vehicle speeds around the circle. The position in the x-axis is defined as starting towards the average wind direction, i.e., position 0, and

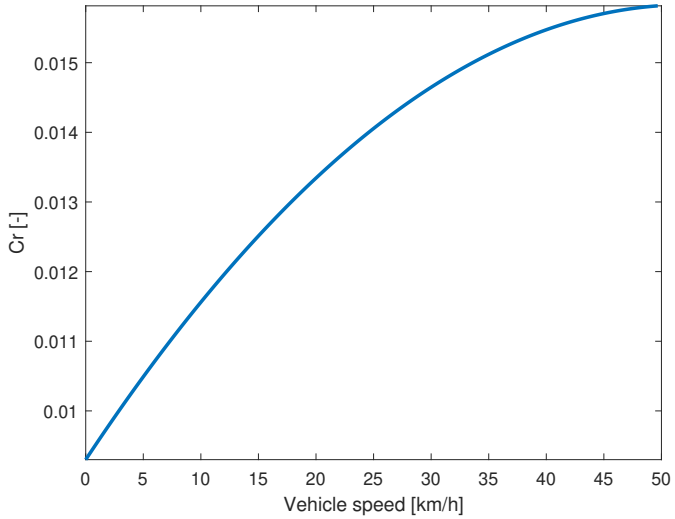

Figure 11. Rolling resistance as function of vehicle speed at low ambient temperature conditions.

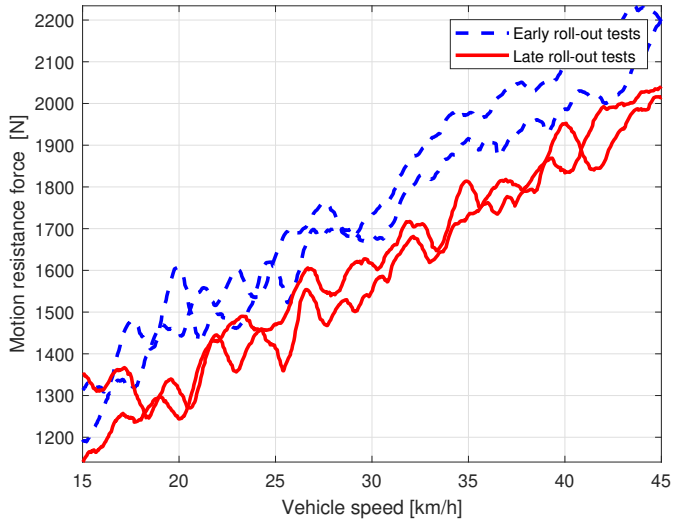

Figure 12. Comparison between early and late roll-out tests.

all integer number of laps, 1,2.., means driving in the headwind direction. Hence, a tailwind will occur in positions 0.5, 1.5, 2.5, etc.

The model is capable of delivering a reasonably accurate measure of the total vehicle motion resistance force in all circle tests. The dominant force in all tested vehicle speeds was the rolling resistance. However, a periodic behavior of the motion resistance force can be observed, especially when going a bit faster. This is the influence of the wind.

In figure 14, the total motion resistance force is plotted together with the modeled motion resistance force from (8), and two variants of the base model (3). The two base models use constant terms for ρ, and C_r and assume zero wind conditions and are hence using $C_dA = C_dA(0)$ and $v_{ax} = v_v$. One base model uses data found in the literature corresponding to ambient conditions around $20°C$, with $\rho = 1.21$ kg/m^3 and $C_r = 0.007$. The value of C_r is motivated from being somewhere in the middle of assumptions on C_r used in other studies where C_r typically spans from 0.0045 to

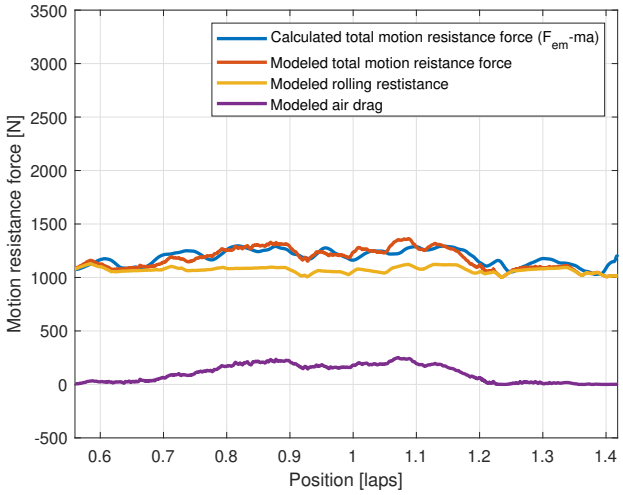

(a) 10 km/h

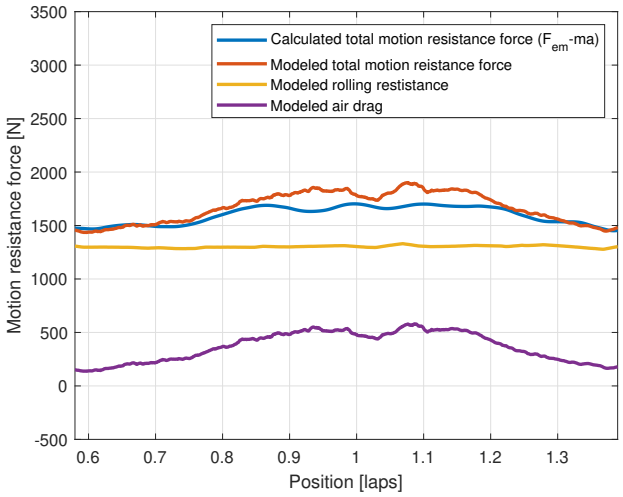

(b) 30 km/h

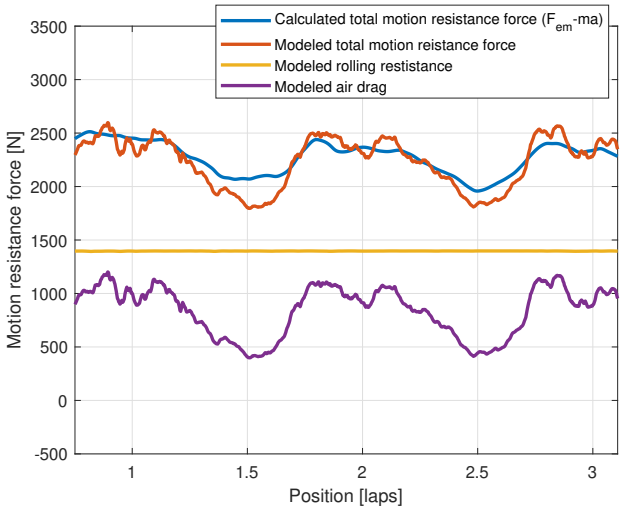

(c) 50 km/h

Figure 13. Calculated and modeled motion resistance force components using wind speed measurements.

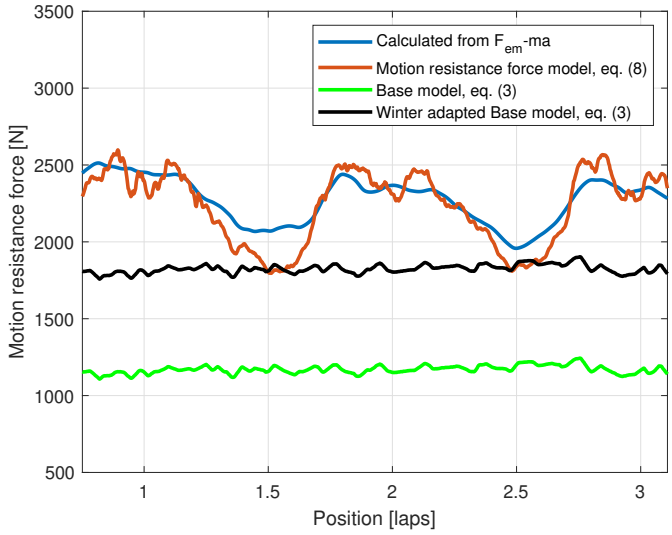

Figure 14. Comparison of motion resistance force models. Vehicle speed = 50 km/h.

0.01, e.g. [21–23]. For the other base model, from now on denoted winter-adapted base model, the air density is set to the computed air density during the tests ($\rho = 1.29$ kg/m^3) and $C_r = 0.014$ is chosen to correspond to the rolling resistance from the developed empirical model when running in $v_v = 25$ km/h.

The winter-adapted base model clearly improves the motion resistance model, as shown in figure 14. It gets the motion resistance to a base level that is not very far from the resistance in zero-wind conditions. However, to be able to model changes that occur due to the current specific road weather situation, this model is not sufficient. The proposed full motion resistance model can capture the changes in wind conditions that occur when going around the ice circle.

In table 3, the root mean square deviations between the calculated total motion resistance force and the same force modeled with the full motion resistance model and the two base models are given. As can be seen, the full motion resistance model is always performing better than the two base models and the winter adapted base model is always better than the base model without the adaptations. The root mean square error is also increasing with the vehicle speed which is expected since the magnitude of the motion resistance also increases with the vehicle speed. There is one exception, though. The winter-adapted base model shows a lower root mean square error in 20 km/h than in 10 km/h. This can be explained by the fact that the winter adaptation of C_r was done to match the model rolling resistance at the vehicle speed = 25 km/h. This means that the winter-adapted rolling resistance model will likely perform better when the vehicle speed is close to 25 km/h.

5. Discussion

A motion resistance model for winter conditions that includes effects from varying wind conditions was developed using measurements from a battery electric truck equipped with a wind sensor and a TPMS system. The wind speed measurements were calibrated using data from ice-circle tests through an optimization scheme where the wind was assumed to be constant during the measurements. The modeled motion resistance

Table 3. Benchmark example. Comparing root mean square errors for the baseline model proposed in the literature, with and without adaptation to winter conditions, and the proposed model at different speeds.

	Vehicle speed				
Model	10 km/h	20 km/h	30 km/h	40 km/h	50 km/h
Base (3)	530 N	670 N	750 N	880 N	1100 N
Winter (3)	110 N	79 N	160 N	260 N	480 N
Model (8)	65 N	72 N	84 N	86 N	130 N

force shows overall good conformity with a motion resistance force computed from electric machine power and vehicle speed and acceleration during ice circle tests.

The development of the motion resistance model was difficult due to the lack of measurements of individual motion resistance forces in combination with uncertainties in the measurement data. To begin with, both the rolling resistance and the air drag force models used, (6) and (5) respectively, are vehicle speed dependent which makes it difficult to separate the parameters of those two models. However, the C_D parameter of the air drag model is chosen to match the C_dA value computed from CFD simulations for $\theta = 0°$, as can be seen in figure 9. This value is also close to what was found from wind tunnel tests performed with vehicles with the same type of chassis. This should assure the confidentiality of the model in terms of air drag from vehicle speed and pure head/tail wind components, i.e., $C_dA(\theta = 0)$.

For the model for air drag induced by crosswinds, the ice circle tests were used to verify its legitimacy. Those tests were performed on a fairly homogeneous road surface (scraped ice) and at close to constant speed. This implies that the variations seen in the motion resistance during each of these tests are due to changes in wind-induced air drag. The relatively good model fit during these tests suggests that the air drag model should be regarded as fairly accurate with respect to crosswind. There is a risk, though, that unless the wind speed measurement is perfect, an error in the wind measurement may inflict minor errors in the air drag model.

The calibration of the wind speed measurements was done independently of the air drag model. The calibrated wind speed behaves almost as expected when going around the circle, as visualized in Figure 7. The expectation is that when going around a circle with fairly constant wind, both the headwind and crosswind speed components should have the shape of a sine curve. At times close to 80, 180, and 280 seconds, the truck moves towards the wind, and the expected headwind component should peak. This is not really the case, and instead, the headwind component has an oscillating behavior. This could be due to changes in the wind, but since it is repeated several times, it is more likely that there is some turbulence in the air around the sensor, creating somewhat unreliable readings when $\theta \approx 0°$. Nevertheless, the ability to follow the changes in air drag when going around the circle demonstrated in figure 13 shows that potential errors from the wind measurements are relatively small.

The linear calibration scheme in longitudinal vehicle speed and wind direction was shown to have flaws for large air attack angles, typically $\theta > 45°$. However, those large air attack angles will only occur at low vehicle speeds unless wind speeds are extremely high. For the underlying range prediction problem, errors in wind information when going at such low vehicle speeds are only important in extreme wind conditions due

to the low air drag that otherwise occurs.

The remaining motion resistance force component in the model is the rolling resistance. The rolling resistance model was calibrated using measurements from the roll-out tests. These measurements found the rolling resistance force by withdrawing the air resistance from an estimated motion resistance force. The estimated motion resistance force was found using (1) where m was assumed to be known and F_{trac} was calculated from the total electrical machine power and vehicle speed. The first thing to notice here is that with this model, the rolling resistance force will contain components often not included in the rolling resistance. Examples of this are the losses in the wheel bearings and electric machine idle losses. This does not change the validity of the overall motion resistance model but may cause the rolling resistance coefficient to appear to be a bit higher when compared to other studies.

The second thing to notice is that by using this methodology, errors in the air drag model will inflict errors in the rolling resistance model as well. The errors in the rolling resistance model will at least partly compensate for the errors in the air drag model. The result of this may be that the motion resistance model works well during the tested conditions but will not be applicable for other operating conditions since then, the errors in the rolling resistance model and air drag models may not even out anymore. However, looking at figure 10, the contribution from vehicle speed was the dominant component of the air drag during the roll-out tests used for the rolling resistance modeling. As discussed in a previous section, the air drag component from vehicle speed is judged to be reliable. The uncertain component is the wind-induced air drag which had a very low magnitude during the roll-out tests compared to the rolling resistance. This gives a favorable signal-to-noise ratio and hence, the rolling resistance model should be fairly reliable as well.

Others have also conducted rolling resistance tests in winter climates. In a recent paper, [20], it is suggested that the rolling resistance follows a master curve where the rolling resistance coefficient merely depends on the tire temperature. The vehicle speed dependency is instead described as a horizontal shift of the tire temperature. Such a model may be able to capture the observed drift in rolling resistance during the tests that was assumed to be due to tire temperature drift. The tires of the test vehicle were equipped with sensors measuring the tire temperature close to the rim. However, as noticed in [20], the tire temperature is not homogeneous and differs greatly between different parts of the tires. A drift in tire temperatures was noticed, but the dynamics did not match the rolling resistance drift. Therefore, the tire temperature was left out from the rolling resistance model. This is, however, something we intend to investigate in future works.

It is worth pointing out that the developed empirical rolling resistance model is only valid for the prevailing operating conditions during the data collection. Rolling resistance is highly dependent on tire temperature. If applying the proposed motion resistance model to the range estimation problem, adaptations to the anticipated road surface conditions are vital, as well as adaptations to the heat-up of the tires that occurs during the operations. For a laden truck, the tire heat-up is considerable. Therefore, the true rolling resistance coefficient is likely to be significantly lower than what is given from the empirical rolling resistance model without adjustments but far from as low as it would be during summer conditions. To develop a rolling resistance model that includes the temperature dynamics is left for future work.

The implication of the results in this investigation is that range prediction algorithms need to take weather information into account. Failing to do so will inevitably lead to an overestimated range during winter conditions that can cause severe prob-

lems in unwanted stops and prolonged transportation times due to longer charging time than expected. This also implies that high-quality road weather information is needed. What information that is needed to be able to accurately predict rolling resistance energy consumption and how to acquire that information are also left for future work.

6. Conclusions

The main conclusion of this work is that it is crucial to take weather into account when doing range predictions, as motion resistance is greatly affected by the weather conditions. In the conducted winter tests, it was shown that the motion resistance force is affected by several different weather components. When adapting the base model to winter conditions, the overall model accuracy is vastly improved. Furthermore, the magnitude of the rolling resistance coefficient in cold climates was shown to depend on vehicle speed in the tested conditions. Additionally, the air drag model captures the wind effect more realistically than the base model usually used in longitudinal vehicle dynamics simulations or range prediction algorithms. Altogether, the developed motion resistance model was considerably more accurate than the base model in changing wind conditions and at different vehicle speeds. Furthermore, the model is simple enough for a range prediction algorithm.

7. Acknowledgments

The authors would like to thank the Swedish Energy Agency for funding part of this investigation via the U-FEEL project, Project ID: P2022-00948.

References

[1] ACEA. FACTSHEET CO2 STANDARDS FOR HEAVY-DUTY VEHICLES. https://wwwaceaauto/files/Fact-sheet-CO2_standards_for_heavy_duty_vehiclespdf. 2023;Available from: `www.acea.auto`.

[2] European Commission. 2050 low-carbon economy — Climate Action. http://eceuropaeu/clima/policies/strategies/2050_en. 2017;Available from: `http://ec.europa.eu/clima/policies/strategies/2050_en`.

[3] Lebeau K, Mierlo JV, Lebeau P, et al. Consumer attitudes towards battery electric vehicles: a large-scale survey. Int J Electric and Hybrid Vehicles. 2013;5(1):28–41. Available from: `http://mobi.vub.ac.be`.

[4] Cunanan C, Tran MK, Lee Y, et al. A Review of Heavy-Duty Vehicle Powertrain Technologies: Diesel Engine Vehicles, Battery Electric Vehicles, and Hydrogen Fuel Cell Electric Vehicles ; 2021.

[5] Bailey C, Jones B, Clark M, et al. Electric Vehicle Autonomy: Realtime Dynamic Route Planning and Range Estimation Software. In: IEEE Conference on Intelligent Transportation Systems, Proceedings, ITSC; Vol. 2022-October. Institute of Electrical and Electronics Engineers Inc.; 2022. p. 2696–2701.

[6] Gupta A, Hu S, Zhong W, et al. Road grade estimation using crowd-sourced smartphone data. In: Proceedings - 2020 19th ACM/IEEE International Conference on Information Processing in Sensor Networks, IPSN 2020; 4. Institute of Electrical and Electronics Engineers Inc.; 2020. p. 313–324.

[7] Janssen ML, Hall GL. Effect of Ambient Temperature on Radial Tire Rolling Resistance. Source: SAE Transactions. 1980;89:576–580. Available from: https://www.jstor.org/stable/44632443?seq=1&cid=pdf-reference#references_tab_contents.
[8] Ydrefors L, Hjort M, Kharrazi S, et al. Rolling resistance and its relation to operating conditions: A literature review. Proceedings of the Institution of Mechanical Engineers, Part D: Journal of Automobile Engineering. 2021 10;235(12):2931–2948.
[9] Jones FE. The Air Density Equation and the Transfer of the Mass Unit. JOURNAL OF RESEARCH of the Notional Bureau of Standards. 1978 9;83(5):419–428.
[10] Abel R, Pegel L, Waldmann A. On the Importance of Highly Resolved Wind Forecasts for Range Estimation. In: Internationales Stuttgarter Symposium. Springer Vieweg, Wiesbaden; 2022. p. 187–196.
[11] Hua L, Tang J, Dourra H, et al. A Grey-Box Surrogate Vehicle Energy Consumption Model Capable of Real-Time Updating. In: 3 IEEE/ASME International Conference on Advanced Intelligent Mechatronics (AIM); 2023.
[12] Baker CJ. A simplified analysis of various types of wind-induced road vehicle accidents. Nottingham: Nottingham University, Department of Civil Engineering; 1986.
[13] Askerdal M, Fredriksson J, Laine L. Development of simplified air drag models including crosswinds for commercial heavy vehicle combinations. Vehicle System Dynamics. 2023 5;:1–18Available from: https://www.tandfonline.com/doi/full/10.1080/00423114.2023.2213786.
[14] Kim Y, Guanetti J, Borrelli F. Compact Cooperative Adaptive Cruise Control for Energy Saving: Air Drag Modelling and Simulation. IEEE Transactions on Vehicular Technology. 2021 8;70(10):9838–9848. Available from: http://arxiv.org/abs/2108.07911.
[15] Hamednia A, Murgovski N, Fredriksson J, et al. Optimal Thermal Management, Charging, and Eco-driving of Battery Electric Vehicles. IEEE Transactions on Vehicular Technology. 2023 6;.
[16] Vo-Duy T, Doan TM, Nguyen BH, et al. Optimal Energy Management System of Dual-motor Electric Vehicles with Longitudinal Dynamic Characteristic Consideration. IEEE Transactions on Vehicular Technology. 2023;.
[17] Mars WV, Luchini JR. An Analytical Model for the Transient Rolling Resistance Behavior of Tires. Tire Science and Technology. 1999 7;27(3):161–175. Available from: http://meridian.allenpress.com/tst/article-pdf/27/3/161/1974629/1_2135982.pdf.
[18] Nielsen L, Sandberg T. A New Model for Rolling Resistance of Pneumatic Tires. JOURNAL OF PASSENGER CAR: MECHANICAL SYSTEMS JOURNAL. 2002;111:1572–1579. Available from: https://www.jstor.org/stable/44719334.
[19] Schuring DJ, Siegfried JF. Transient Speed and Temperature Effects on Rolling Loss of Passenger Car Tires. Hall Source: SAE Transactions. 1985;94:515–523. Available from: https://www.jstor.org/stable/44721587.
[20] Hyttinen J, Ussner M, Österlöf R, et al. Truck tyre transient rolling resistance and temperature at varying vehicle velocities - Measurements and simulations. Polymer Testing. 2023 5;122.
[21] Yildirim M, Kurt S. Effect of Different Types of Electric Drive Units on the Energy Consumption of Heavy Commercial Electric Vehicles. World Electric Vehicle Journal. 2022 5;13(5).
[22] Stegner E, Snitzer P, Bevly D, et al. New Metrics for Quantifying the Energy Efficiency of Platoons in the Presence of Disturbances. In: SAE Technical Papers. SAE International; 2022.
[23] Basma H, Beys Y, Rodríguez F. Battery electric tractor-trailers in the European Union: A vehicle technology analysis. Retrieved from the International Council on Clean Transportation. 2021;Available from: www.theicct.org.